

Article

Thermodynamic Analysis and Experimental Study of Selective Dehydrogenation of 1,2-cyclohexanediol over $\text{Cu}_{2+1}\text{O}/\text{MgO}$ Catalysts

Haiou Wang ¹, Qiusheng Yang ^{1,2,*}, Yucong Song ¹ and Yanji Wang ^{1,2,*}

¹ School of Chemical Engineering, Hebei University of Technology, Tianjin 300130, China; wanghaiou@hebut.edu.cn (H.W.); yucong0508@163.com (Y.S.)

² Hebei Province Technology Institute of Green Chemical Industry, Hebei University of Technology, Tianjin 300130, China

* Correspondence: yqiusheng@hebut.edu.cn (Q.Y.); yjwang@hebut.edu.cn (Y.W.)

Received: 21 January 2019; Accepted: 9 February 2019; Published: 10 February 2019



Abstract: The dehydrogenation of 1,2-cyclohexanediol (CHD) helps in the effective utilization of not only fossil derivatives but also vicinal diols and polyols from sustainable biomass-derived resources. A thermodynamic analysis of CHD dehydrogenation was computed with density functional theory (DFT) calculation using Gaussian 09. The result indicates that CHD can be converted to 2-hydroxy cyclohexanone (HCO), 2-hydroxy-2-cyclohexen-1-one (HCEO) and pyrocatechol depending on the degree of dehydrogenation. HCO and HCEO are the stable products of the primary and secondary dehydrogenation. Experimentally, Cu/MgO catalysts were prepared using glucose as a reductant, and were characterized by SEM, TEM, XRD, XPS, TPR, BET and ICP. Furthermore, their catalytic performance regarding the oxygen-free dehydrogenation of CHD was investigated. The results indicate that the primary active crystalline phase of Cu/MgO was Cu_{2+1}O , and that the dehydrogenation products were mainly HCO and HCEO, in accordance with thermodynamic predictions. Upon optimizing the reaction conditions, the total selectivity of HCO and HCEO exceeded 90% and the conversion of CHD was approximately 95%.

Keywords: 1,2-cyclohexanediol; $\text{Cu}_{2+1}\text{O}/\text{MgO}$; dehydrogenation; 2-hydroxy cyclohexanone; 2-hydroxy-2-cyclohexen-1-one

1. Introduction

In recent years, the process of producing cyclohexene via the selective hydrogenation of benzene has greatly matured [1–4], having laid a critical foundation for the efficient use of coal. It has been reported that a variety of essential chemical products can be developed from the oxidation of cyclohexene, such as 1,2-cyclohexanediol (CHD), cyclohexane oxide, adipic acid [5–7] etc. More specifically, CHD can be refined into pyrocatechol [8,9], adipic acid [10,11], cyclohexanone [12], and heterocyclic compounds [13–15], etc. Currently, the prevalent studies on the dehydrogenation of CHD rely on stoichiometric oxidants, such as $\text{NaBrO}_3/\text{NaHSO}_3$ [16], O_3 , O_2 [17,18], KMnO_4 , K_2CrO_4 , tert-butyl hydroperoxide [19] and H_2O_2 [20], etc. The primary product produced from the dehydrogenation of CHD is 2-hydroxy cyclohexanone (HCO), but CHD can be further dehydrogenated to form other products (e.g., 1,2-cyclohexanedione and adipic acid [16]) either under excess oxidant concentration, a prolonged reaction time or a high reaction temperature. For example, Vermaet et al [20] used $\text{PEG}\cdot\text{KBr}_3$ to catalyze the dehydrogenation of CHD, by which the CHD in H_2O_2 can be oxidized to HCO or cyclohexanedione by tuning the reaction temperature and the ratio of reactants. In acetonitrile, CHD can be converted into cyclohexanedione, HCO and adipic acid catalyzed by $\text{Q}_3\text{H}_2[\text{IMo}_6\text{O}_{24}]$ ($\text{Q} = (\text{n-Bu})_4\text{N}^+$) at 80 °C [21]. Furthermore, in the presence of excessive oxidants, this not only resulted

in a variety of byproducts, but also recycled excessive oxidants difficultly. Lastly, an excessive number of oxidants increased the likelihood of an explosion via a massive exothermic process.

A possible solution for mitigating this setback was to undergo oxygen-free dehydrogenation. Research into the oxygen-free dehydrogenation of CHD has mainly focused on nickel-based [8] and palladium-based [9] catalysts, while the main product, pyrocatechol, was formed by the deep dehydrogenation of CHD. Few papers have reported the oxygen-free dehydrogenation of CHD to HCO. Sato et al. studied the synthesis of HCO from CHD by oxygen-free dehydrogenation over an Ir-ReO_x/SiO₂ catalyst with an HCO yield of 24.7% at 493 K for 1.0 h [22]. Although the Cu-based catalyst was also an important catalyst, which has been widely used in the dehydrogenation of alcohols [23], it has not been reported in the oxygen-free dehydrogenation of CHD to HCO or 2-hydroxy-2-cyclohexen-1-one (HCEO). The main active components of Cu-based catalysts are Cu⁰ and Cu⁺, the latter possessing better activity and selectivity. Especially at higher temperatures, Cu⁰ will increase the yield of the phenol byproduct [24–27]. In addition, both dehydrogenated intermediates of CHD, CHO and CHEO are not only used as raw material for adipic acid synthesis but are also common building blocks for asymmetric and heteropoly cyclic compounds [28–32]. Thus, it is crucial to investigate the controlled dehydrogenation of CHD to HCO and HCEO over Cu-based catalysts. Furthermore, the dehydrogenation of CHD as a model compound can play an indispensable role for the effective utilization of environmentally-friendly and sustainable resources, since vicinal diols and polyols are common moieties in biomass-derived molecules.

In this work, the reaction thermodynamics of CHD oxygen-free dehydrogenation was computed by Gaussian 2009 at the B3LYP/6-31G+(d, p) level for the preliminary screening of the stability of the possible products. Then, the highly reactive Cu/MgO catalysts were prepared by the impregnation and precipitation method, and were characterized by SEM, TEM, XRD, XPS, TPR, BET and ICP techniques. Lastly, their catalytic performance for dehydrogenating CHD was evaluated on a fixed-bed reactor.

2. Materials and Methods

2.1. Preparation of Cu/MgO Catalyst

Cu/MgO was prepared by two different methods. (1) Precipitation method: One hundred milliliters of 4.0M NaOH solution was quickly added into a 500 mL three-necked flask containing 100 mL of 2.0M Mg(NO₃)₂ solution under vigorous stirring at 80 °C. After stirring for 30 min, 1.0 M Cu(NO₃)₂ solution and 1.0 M glucose solution were added dropwise into the flask. Subsequently, the pH value was adjusted to about 10~11 by the slow addition of a 1.0 M aqueous solution of NaOH, followed by a 1.0 h continuous reduction reaction. Then, the mixture was filtered and the precipitate was washed with ethanol and water three times each. Finally, the precipitate was dried at 110 °C for 12.0 h, and subsequently calcined for 3 h to form *x*Cu/MgO-C-T catalyst (where *x* is the mass ratio of Cu to MgO, C represents the precipitation method, T is the calcination temperature). (2) Impregnation method: The precipitation of Mg(OH)₂ prepared by the above method was first calcined at 400 °C to form an MgO support. The MgO support was then impregnated into the 1.0 M Cu(NO₃)₂ solution for 24 h. Next, the samples were treated similarly to that of the precipitation method; i.e., reduced by NaOH and glucose solution, filtrated, washed, dried and calcined for 3.0 h to form *x*Cu/MgO-IM-T (where IM represents the impregnation method).

All the reagents above were analytical grade and purchased from Bodi Chemical Reagent Factory Co. Ltd., Tianjin, China.

2.2. Catalyst Characterization

X-ray diffractometry (XRD): The crystalline phases of samples were detected by a D/MAX2RB X-ray diffractometer (Rigaku International Corporation, Japan) with monochromatic Cu K α radiation. The scan range spanned from 5° to 90° at a rate of 4° /min.

Scanning electron microscopy (SEM): SEM was performed with an EGA TS-5130SB scanning electron microscope (TESCAN, Czech). The micrographs were obtained at an accelerating potential of 15 kV under low vacuum.

High resolution transmission electronic microscopy (HRTEM): The size and distribution of samples were conducted by using a Tecnai G2 F20 high resolution transmission electronic microscope (FEI, Netherlands) with a point resolution of 0.248 nm and a linear resolution of 0.248 nm. The maximum enlargement factor of this equipment was 1.05 million.

Specific surface area analysis.: The specific surface area of samples was obtained from an N₂ adsorption–desorption isotherm at 77 K with a Micromeritics ASAP 2020 Surface Area and Porosity Analyzer (Micromeritics Instrument Corp., USA), after degassing at 200 °C and 10 µmHg for 4 h. Multipoint BET analysis method was used to calculate the specific surface area.

Temperature-programmed reduction (H₂-TPR):. TPR tests were carried out on Micromeritics Auto Chem II-2920 Chemisorption Analyzer (Micromeritics, USA). The samples were pretreated in a flow of Ar (50 mL/min) at room temperature for 1.0 h. Subsequently, the gas flow was switched to H₂ (10 vol% in Ar, 50 mL/min) and the sample was heated to 900 °C at a ramp rate of 10 °C/min. The H₂ consumption was monitored by a thermal conductivity detector (TCD).

X-ray photoelectron spectroscopy (XPS) and Auger electron spectroscopy (AES): XPS and AES of samples were performed with an HI-1600 X-ray photoelectron microscope (PE, USA) with a monochromatic Mg K α radiation (1253.6 eV) as the X-ray excitation source. The energies of the full spectrum and the narrow spectrum were 187.8 eV and 23 eV, respectively. The binding energy of C1s (284.6 eV) was used as a calibration standard.

Inductively coupled plasma-atomic emission spectrometry (ICP-AES): The elemental composition of the catalysts was determined by ICP-AES on an Optima 7300 V spectrometer (PE, USA).

2.3. Evaluation of Catalytic Activity

The catalytic performance of catalysts for the dehydrogenation of CHD was evaluated on a fixed-bed reactor composed of a stainless-steel tube with an inner diameter of 5 mm. The operational process was as follows: 1.0 g of catalyst and an equal volume of quartz sand were mixed and packed in the thermostatic zone of the reactor. Then, the feed of CHD solution (25 mg CHD/mL tetrahydrofuran) was pumped into the reactor after the catalyst bed was heated to the reaction temperature, and the system pressure was maintained at 0.5 MPa with N₂. During the reaction process, sampling was regularly withdrawn for quantitative analysis.

The reaction products were quantitatively analyzed on a SP3400 gas chromatograph (Beijing Beifen Ruili Analytical Instrument co. Ltd, China) with a PEG-20M capillary column. The analysis conditions were as follows: N₂ carrier gas was flowed at a rate of 30 mL/min, a FID (Flame Ionization Detector) temperature of 220 °C, and an injection port temperature of 220 °C. The column temperature was programmed as follows: the initial oven temperature was set at 80 °C and then increased at a rate of 10 °C·min⁻¹ to 240 °C and then held for 3 min. Lastly, the conversion of CHD and the yield of products were calculated by using the area normalization method.

2.4. Calculation of Thermodynamics

Gaussian 09 software was used to thermodynamically evaluate the dehydrogenation reaction at the B3LYP/DFT level [33]. All atoms were determined by the 6-31G+(d, p) basis set. The solvent effect was calculated by using the polarized continuum model (PCM) [34]. The geometry optimization and frequency were calculated to avoid the emergence of an imaginary frequency in the same methods, which referred to each species. If not noted otherwise, the thermal enthalpies (ΔH) and free energies (ΔG) of the reaction reported in this article were estimated at the relative energies, which refer to those with zero-point energy (ZPE) correction.

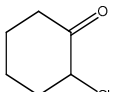
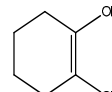
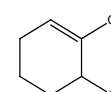
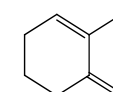
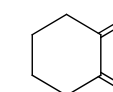
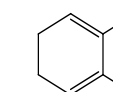
3. Results and Discussion

3.1. Thermodynamic Analysis

3.1.1. Stability Analysis of Primary Dehydrogenation Products

Density functional theory (DFT) calculations were used to predict the possible isomers of the dehydrogenated products. Meanwhile, the thermal equilibrium of dehydrogenation was also calculated. The possible dehydrogenated products and corresponding calculations are summarized in Table 1.

Table 1. ΔG of different isomers of dehydrogenation products.

T (°C)	Primary Dehydrogenation Product (kcal/mol)			Secondary Dehydrogenation Product (kcal/mol)		
						
25 ^a	0.00	17.52	23.15	0.00	5.75	30.00
100 ^a	0.00	13.89	18.43	0.00	4.33	23.84
220 ^a	0.00	10.35	18.26	0.00	3.91	23.56
25 ^b	0.00	18.71	23.72	0.00	0.91	30.04
25 ^c	0.00	18.98	24.25	0.00	0.71	30.04

^a Gas phase; ^b acetonitrile solvent; ^c water solvent.

The products of primary dehydrogenation generate three possible isomers, and their corresponding Gibbs free energies are compiled in Table 1. According to the Arrhenius formula, at 25 °C and under 1 atm, the molar ratio of these three isomers is 10E(+10):2.5E(+3):8.8, which indicates HCO would be the dominant structure, accounting for more than 99.9% of all products. The secondary dehydrogenation products also generate three possible isomers. Likewise, at 25 °C and under 1 atm, the ratio of these three isomers is 10E(+13):3.1E(+11):9.4 according to the Arrhenius formula, which shows that HCEO accounted for over 99% of the formed products. Moreover, when the temperature of the gas phase of the system rises to at least 100 °C, the cyclohexadione isomer occupies only about 1~4% of all structures. In short, these *o*-diketone structures are not very stable in the gas phase. In addition, in either an acetonitrile or water solvent, cyclohexadione occupies 32% and 29%, respectively, of the total secondary products. Due to the conjugation nature of HCEO, the carbon–carbon single bond adjoined to the hydroxyl oxygen is not easily broken, whereas the carbon–carbon bond is easily severed owing to the two adjacent ketones, which rationalizes why the carbon–carbon bond of cyclohexadione can be easily oxidized.

3.1.2. Thermodynamic Analysis of the Dehydrogenation Reaction in the Gas Phase

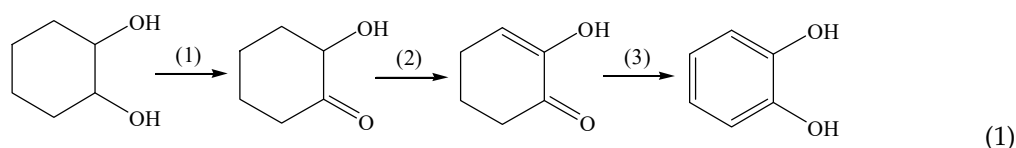
CHD usually produces stable pyrocatechol through deep dehydrogenation. The reaction process is shown in Equation (1). The results of the thermodynamic calculation for the dehydrogenation of CHD are shown in Table 2. This indicates that the three-step dehydrogenation reactions of CHD are all endothermic reactions, in which the amount of heat absorbed from the largest to the smallest is in the order of the second step, then the first step, and then the third step. As the temperature increases, the reaction accelerates, the equilibrium shifts towards the right of the reaction, and the conversion rate increases. Actually, the second step of the dehydrogenation is the most critical step of the entire reaction. In fact, the temperature of the first step will occur spontaneously at about 114 °C; however, the second step occurs only when the temperature exceeds 340 °C, while the last step can occur at least 32 °C. When the first two steps are combined, the temperature of the reaction can occur spontaneously at 227 °C; however, when all three steps are combined, the temperature of the reaction can occur

at 160 °C. Furthermore, at a temperature of 250 °C, the equilibrium conversion rate of the first step reaction will be an impressive 98.3%.

Table 2. The thermodynamic data of the stepwise dehydrogenation reaction in the gas phase.

T (°C)	ΔH (kcal/mol)			ΔG (kcal/mol)		
	(1)	(2)	(3)	(1)	(2)	(3)
25	11.59	18.21	8.97	2.74	9.57	0.15
50	11.70	18.34	9.13	2.00	8.84	−0.60
100	11.89	18.57	9.44	0.48	7.36	−2.13
150	12.05	18.78	9.72	−1.06	5.84	−3.70
200	12.18	18.96	9.98	−2.61	4.30	−5.30
220	12.23	19.03	10.07	−3.24	3.68	−5.94
250	12.30	19.12	10.20	−4.18	2.74	−6.92
300	12.39	19.25	10.40	−5.76	1.17	−8.57

Generally, hydrogen can maintain the oxidation performance of catalysts [35,36]. If the hydrogen amount in the system is up to 10 times that of stoichiometry, the equilibrium conversion rate of the first step will be restricted to 83.7% at 250 °C. Additionally, if the hydrogen in the system is again lowered to 2 times, the conversion rate of the first step will again be limited to 90.4% at 220 °C. The conversion rate of the first step of the dehydrogenation will be at 96.6% at the same temperature under the oxygen-free dehydrogenation condition. Therefore, the hydrogen removed from the system will not affect the reaction obviously; on the contrary, it may also help to keep the catalyst active [8,12].



Additionally, the dehydration reaction is the primary side reaction during the dehydrogenation of CHD [12], which is followed by a ring-opening and fragmentation reaction at higher temperatures. At 220 °C, the free energy of the dehydration step, producing cyclohexanone, is -23.68 kcal/mol, which is far lower than that of the entire dehydrogenation reaction. Therefore, the dehydration needs to be strictly inhibited by a better catalyst. On the other hand, alcoholysis usually involves free radical reactions at higher temperatures. Thus, the reaction temperature should be appropriately controlled in order to decrease pyrolysis products.

3.2. Catalyst Characterization Results

Cu/MgO catalysts with different Cu loadings were prepared by the precipitation method and calcined at 250 °C and 350 °C in an N₂ environment. Their XRD spectra are presented in Figure 1. Compared with the standard charts of JCPDS 76-0667, 45-0946 and 05-0667, 2θ angles of 18.6°, 38.0°, 50.8° and 58.7° were matched with the 001, 011, 012 and 110 crystal face diffraction peaks of Mg(OH)₂, respectively. Furthermore, the 2θ angles of 42.9° and 62.3° were matched with the 200 and 220 crystal face diffraction peaks of MgO, respectively. Lastly, the 2θ angles of 29.3°, 36.5°, 42.3°, 61.3° and 73.4° corresponded to the 110, 111, 200, 220 and 311 crystal face diffraction peaks of Cu₂₊₁O, respectively. These results indicate that Mg(OH)₂ was decomposed into MgO as the temperature increased from 250 °C to 350 °C. In addition, there was no evident crystalline phase of Mg(OH)₂ in the samples calcined at 350 °C, because 350 °C was the lowest temperature for the complete decomposition of Mg(OH)₂ [37]. However, the crystalline phase of Cu₂₊₁O could be detected after being calcined at

temperature of at least 250 °C. Under alkaline conditions (pH = 10~12), glucose can reduce Cu^{2+} to Cu^+ due to its weak reducibility, as shown in Equation (2).

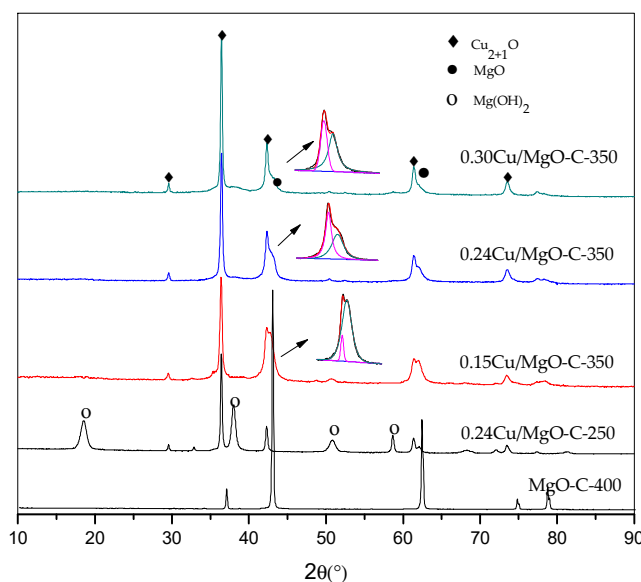


Figure 1. XRD patterns of Cu/MgO catalysts with different Cu loadings.

Elemental Cu mainly existed in the form of crystalline phase of Cu_{2+1}O . Based on the (111) crystal face and Scherrer's equation, the crystallite size of the prepared Cu_{2+1}O at various Cu concentrations was about 30 nm. The SEM images of 0.24Cu/MgO-C-350 and 0.30Cu/MgO-C-350 are shown in Figure 2. It can be seen that the particle size of these catalysts was about 30 nm, which was consistent with the XRD results.

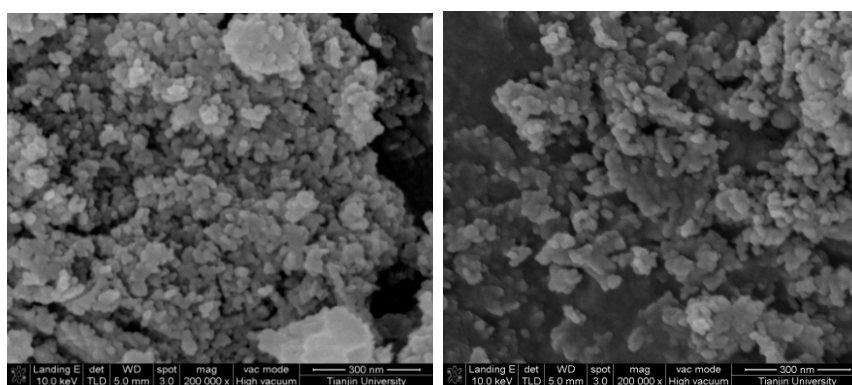


Figure 2. SEM images of catalysts: (a) 0.24Cu/MgO-C-350; (b) 0.30Cu/MgO-C-350.

The Cu/MgO catalysts with different Cu loadings were alternatively prepared by the impregnation method, and their XRD patterns are exhibited in Figure 3. A Cu^0 phase (JCPDS04-0836, $2\theta = 43.3^\circ, 50.4^\circ$) evidently emerges in the samples prepared through the impregnation method [24], which may, compared to the samples prepared by the precipitation method, be due to the presence of more $\text{Cu}(\text{NO}_3)_2$ on the catalyst surface and more contact between the $\text{Cu}(\text{NO}_3)_2$ and glucose. TEM (Figure 4) images affirm the uniform distribution of Cu on the surface of the MgO and the corresponding crystalline grain size of between 20~30 nm.

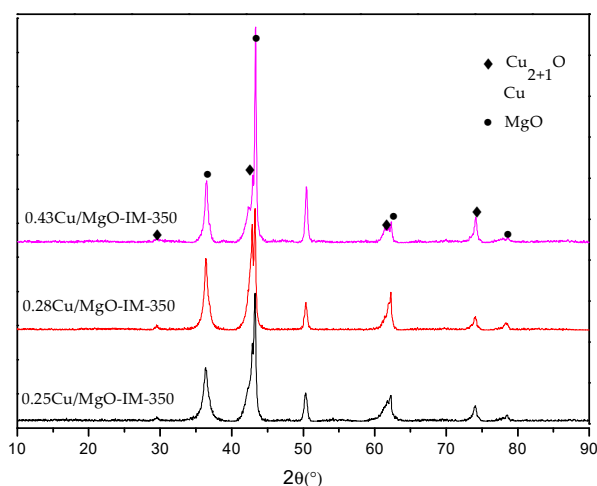


Figure 3. XRD patterns of the Cu/MgO catalysts prepared by impregnation method and calcined at 350 °C.

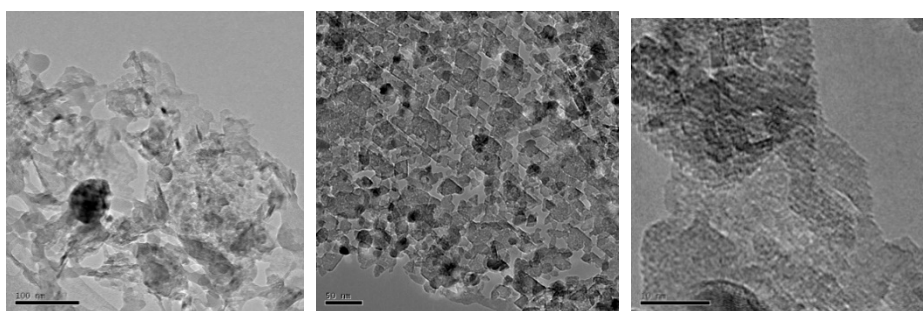


Figure 4. TEM images of the 0.28Cu/MgO-IM-350 catalyst prepared by the impregnation method.

Table 3 summarizes the specific surface area, mass ratio of Cu to MgO and the crystallite sizes of Cu_{2+1}O and MgO of various Cu/MgO catalysts. The composition of the bulk phase of the catalyst was measured by ICP, and the results confirm that the mass ratio of Cu to MgO was preserved from the initial loading to post-synthesis. Furthermore, the specific surface area of the as-prepared Cu/MgO catalysts gradually decreases and the crystallite size of Cu_{2+1}O increases as the Cu-loading increases. The reason for this may be that the Cu component occupied the pore channel of MgO. It can be seen from Table 1 that after the catalyst was heated for 3 h at 350 °C, the sizes of the crystalline grain of Cu_{2+1}O and MgO were 20~40 nm and about 10 nm, respectively. When comparing the different methods of preparing the catalysts, the specific surface area of Cu/MgO prepared by precipitation method is greater than that prepared by the impregnation method. The MgO for the impregnation from $\text{Mg}(\text{OH})_2$ was first calcined at 400 °C for 3 h, which converts the precipitated, amorphous MgO into a crystalline state and greatly decreases its specific surface, while the crystal size for Cu_{2+1}O changed slightly.

Table 3. The composition, crystalline grain size and specific surface area of the catalysts.

Catalysts	Specific Surface Area (m^2/g)	Mass Ratio of Cu to MgO ^a	Crystallite Sizes (nm, XRD)	
			Cu_{2+1}O	MgO
0.14Cu/MgO-C-350	49.3	0.14:1	27.8	8.8
0.24Cu/MgO-C-350	47.4	0.24:1	29.0	8.7
0.30Cu/MgO-C-350	44.6	0.30:1	34.2	11.7
0.28Cu/MgO-IM-350 ^b	29.9	0.28:1	35.2	49.2

^a Measured by ICP; ^b $\text{Mg}(\text{OH})_2$ was firstly calcined at 400 °C for 3 h.

The XPS technique was also employed to characterize the 0.24Cu/MgO-C-350 catalyst, and its corresponding result is presented in Figure 5. Since the binding energy of Cu^0 and Cu^+ is very close and cannot be further deconvoluted, the use of Cu LMM Auger spectrum was instead employed to discriminate between Cu^0 and Cu^+ . There is only one peak (917.3 eV) between 916 eV and 920 eV in Auger electron spectroscopy (not listed), indicating no Cu^0 in the sample [24]. The XPS spectrum of Cu $2p_{3/2}$ was subjected to peak deconvolution to generate two peaks of binding energy at 932.5 eV and 934.8 eV, which correspond to Cu^+ and Cu^{2+} , respectively [38]. Furthermore, the ratio of $\text{Cu}^{2+}/\text{Cu}^+$ was 22.8:100 according to the fractal processing of the Cu $2p_{3/2}$ peaks. Another method used the correlation between the area of the nearest shake-up peak (940–945 eV) of Cu^{2+} and its linear equation of area in Cu $2p_{3/2}$ [38]. The ratio of $\text{Cu}^{2+}/\text{Cu}^+$ was consistent with the former on the whole. However, the binding energy of Cu^{2+} in this sample is higher than that in the literature (the binding energy of Cu $2p_{3/2}$ in CuO is about 933.5 eV), indicating that there is a stronger interaction between Cu^{2+} and MgO or Cu_2O . Furthermore, the $2p \rightarrow 3d$ satellite peak at 940~945 eV further validates the existence of Cu^{2+} species [24].

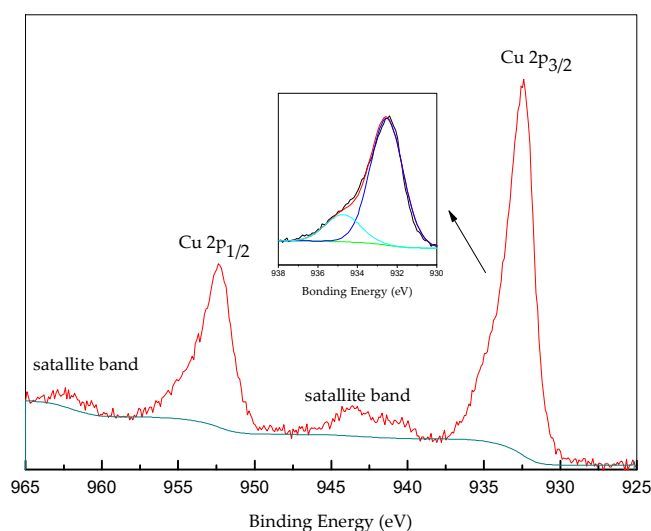


Figure 5. XPS patterns of the 0.24Cu/MgO-C-350 catalyst.

Figure 6 contrasts the H_2 -TPR curves of the Cu/MgO catalysts, and the TPR spectra of the investigated catalysts are significantly influenced by the two different methods. It is apparent that the reduction peak area for Cu/MgO prepared by the precipitation method is significantly larger than that of the Cu/MgO prepared by the impregnation method. From the results of XRD in Figures 1 and 3, the CuO in 0.28Cu/MgO-IM-350 was partially reduced to Cu^0 during the preparation process, while most of the CuO was reduced to Cu^{2+1}O in 0.30Cu/MgO-C-350, which may be responsible for the difference in the reduction of the peak area. As for the H_2 reduction temperature, 0.30Cu/MgO-C-350 reduces at a higher temperature of about 220 °C than that of 0.28Cu/MgO-IM-350, which reduce at 186 °C and 207 °C, respectively, based on the fractal processing of the reduction peak. The temperature is below the reduction temperature of CuO, and the reduction temperature of pure CuO ranges from 500 K to 750 K. The single symmetric reduction peak for the former indicated that it was reduced completely in a single-step. It also reveals that Cu_{2+1}O species in the catalyst are dispersed uniformly with a single structure. The reason for this may be that most of the Cu component exists on the surface for 0.28Cu/MgO-IM-350, and in the bulk phase for 0.30Cu/MgO-C-350, which increases the difficulty of the reduction.

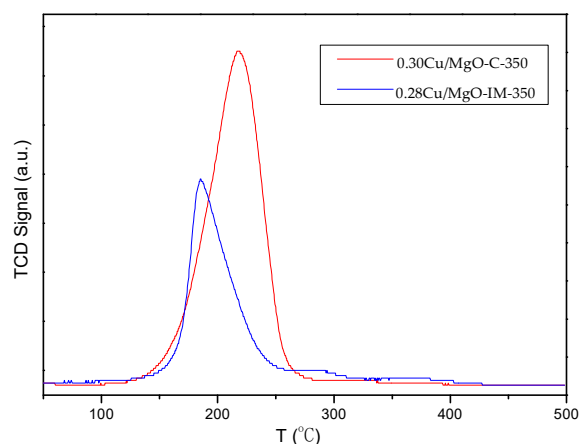


Figure 6. H₂-temperature-programmed reduction (TPR) profiles of Cu/MgO.

3.3. Catalytic Performance of Cu/MgO in the Dehydrogenation of CHD

The qualitative analysis of the dehydrogenation was carried out on a GC-MS. It was discovered that the major components in the CHD dehydrogenation in the presence of Cu/MgO were HCO and HCEO, but the extended dehydrogenation product, pyrocatechol, could not be detected. Other byproducts in the reaction were also detected as expected, such as cyclohexanone, hexanol, etc.

3.3.1. Effects of Preparation Conditions on the Catalytic Performance of Cu/MgO

(1) Effect of Cu loading

Cu/MgO catalysts with different Cu loadings were prepared, and the influence of Cu loading on the catalytic performance is listed in Figure 7. In the absence of Cu, the conversion of CHD was rather low, and the total yield of both HCO and HCEO was also lacking despite the presence of MgO. From this result, it can be surmised that the addition of Cu to MgO is crucial to the dehydrogenation of CHD. As the content of Cu increased, the conversion of CHD also improved. However, the conversion of CHD would decline after exceeding a certain Cu content threshold. More specifically, when the percentage of Cu is optimized between 20~30%, the conversion of CHD can exceed 90% and the yield of the dehydrogenation products, HCO and HCEO, can surpass 85%. However, when the Cu content exceeds 30%, both the conversion rate of CHD and the selectivity of HCO and HCEO would decline, resulting in the increase of other byproducts, such as cyclohexanone and a number of other small molecules.

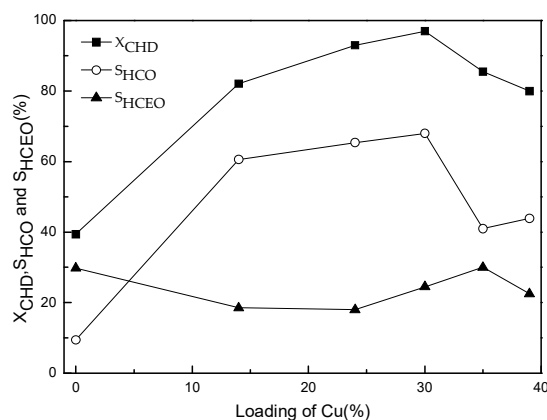


Figure 7. Effect of Cu loading on the catalytic performance of Cu/MgO^a. a. Reaction conditions: N₂ 40.0 mL/min, catalyst 1.0 g, 1,2-cyclohexanediol (CHD) solution 0.05 mL/min, 220 °C.

(2) Effect of calcination temperature

The effect of the calcination temperature on the catalytic performance was also investigated, and the results are summarized in Figure 8. The calcination temperature has a significant effect on the catalytic performance of Cu/MgO. More specifically, catalysts calcined at different temperatures have a lesser effect on the conversion of CHD, but will significantly affect the selectivity of the products. When the calcination temperature is below 350 °C, Mg(OH)₂ and a few hydroxyl groups exist within and on the surface of the catalyst, respectively. Due to the surface hydroxyl groups, there exists a strong adsorption capacity between HCO and the catalyst, which was beneficial to the double dehydrogenation of CHD to HCEO. When the calcination temperature is set between 350 °C and 450 °C, the selectivity of HCO is apparently greater than that of HCEO. However, the selectivity of the product of the double dehydrogenation easily exceeds that of the first dehydrogenation when the catalyst was calcined at 550 °C. Lastly, the total selectivity of both HCO and HCEO significantly decreased because HCEO would further dehydrate into cyclohexanone and other smaller molecules.

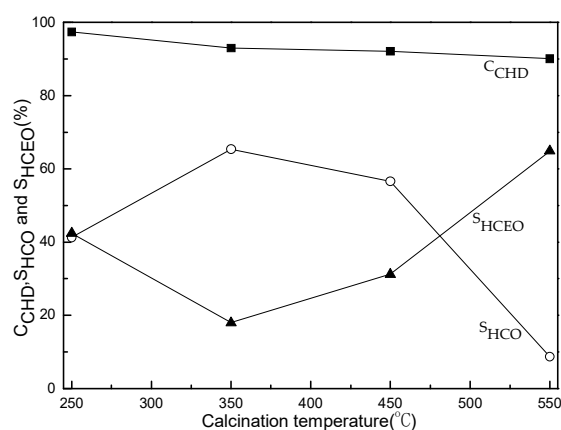


Figure 8. Effect of calcination temperature on the catalytic performance of Cu/MgO^a. a. Reaction conditions: N₂ 40.0 mL/min, catalyst 1.0 g, CHD solution 0.05 mL/min, 220 °C.

3.3.2. Effect of Reaction Conditions on the Dehydrogenation of CHD

(1). The influence of reaction temperature

The effect of reaction temperature on the dehydrogenation of CHD was studied and the results are exhibited in Figure 9. CHD can undergo a dehydrogenation reaction on the surface of the catalyst at 150 °C, and the selectivity of HCO and HCEO are essentially equal. However, as the reaction temperature increases, initially, both the conversion of CHD and selectivity of HCO will increase while the selectivity of HCEO will decline because HCO desorbs more easily from the catalyst surface at higher temperatures. In addition, when the reaction occurs below 300 °C, the sum of the selectivity of HCO and HCEO eclipses 85%. However, at a reaction temperature of 300 °C, the CHD conversion and HCO selectivity declines sharply. This decline in the catalytic activity can be attributed to the formation of carbon deposits on the catalyst and the decomposition of CHD into smaller molecules. Thus, the optimal reaction temperature was reckoned to be 220 °C.

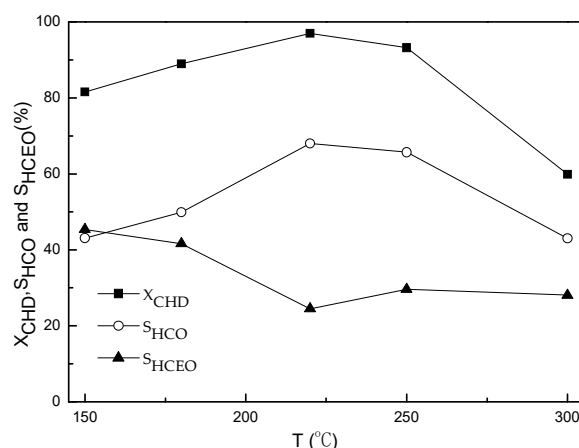


Figure 9. Effect of reaction temperature on the dehydrogenation of CHD^a. a. Reaction conditions: N₂ 40.0 mL/min, 0.30Cu/MgO-C-350 1.0 g, CHD solution 0.05 mL/min.

(2). Effect of N₂ flow rate

In fixed-bed reactors, inert gases are incorporated as carrier gases to dilute the active material of interest. The effect of the N₂ flow rate was studied and the results are reported in Figure 10. As seen, the CHD conversion and HCO selectivity initially increased, then decreased during the gradual increase of N₂ flow. This can be explained by the poor material dispersion at lower N₂ flow rates, which led to the low conversion of CHD and the slow desorption rate of HCO from the catalyst surface. As a result, there is a comparatively higher selectivity of HCEO. When the N₂ flow rate increased to 40 mL/min, the CHD conversion and HCO selectivity reached their maxima at 97.0% and 68.0%, respectively, while the selectivity of HCEO decreased to 24.5%. From this perspective, increasing the N₂ flow rate caused the CHD conversion, HCO selectivity and HCEO selectivity to decrease because the residence time was apparently too short for this reaction.

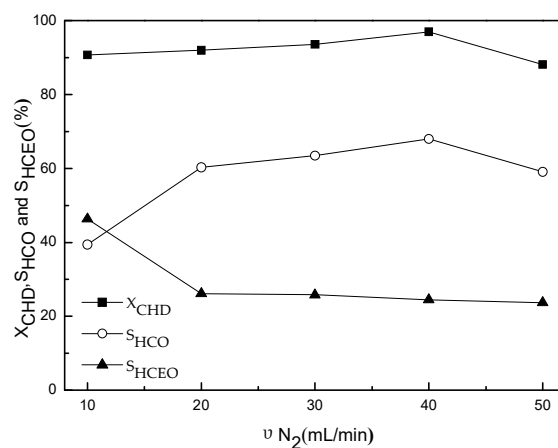


Figure 10. Effect of the N₂ flow rate on the dehydrogenation of 1,2-cyclohexanediol^a. a. Reaction conditions: 0.30 Cu/MgO-C-350 1.0 g, CHD solution 0.05 mL/min, 220 °C.

4. Conclusions

(1) The thermodynamic analysis of CHD dehydrogenation was conducted by DFT. HCO, HCEO and pyrocatechol were produced from the dehydrogenation reaction. The three steps of CHD dehydrogenation were all endothermic, in which the heat absorption of the second step was the largest.

(2) Cu/MgO catalysts were prepared with glucose as the reductant to catalyze the oxygen-free dehydrogenation of CHD. The Cu₂₊₁O phase is the main catalytic site, and the strong interaction

between Cu_{2+1}O and MgO is also beneficial to the reaction. Cu/MgO has a high catalytic selectivity towards HCO and HCEO , but no pyrocatechol was formed over $\text{Cu}_{2+1}\text{O}/\text{MgO}$ catalysts. The highest yields of HCO and HCEO were 68.0% and 24.5%, respectively, while the highest conversion rate of CHD was 97.0%.

This study provides both high value-added chemicals and environmentally-friendly hydrogen energy. The above routes can also be used in the dehydrogenation of renewable polyhydroxy biomass.

Author Contributions: Conceptualization and methodology, H.O.; software and data curation, Q.S.; investigation, Y.C.; writing—original draft preparation, H.O.; writing—review and editing, Q.S.; supervision and funding acquisition, Y.J.

Funding: This research was funded by the National Natural Science Foundation of China, grant number 21236001.

Conflicts of Interest: The authors declare no conflicts of interest.

References

1. Zhou, G.; Dong, Y.; Jiang, L.; He, D.; Yang, Y.; Zhou, X. Effect of support composition on the structural and catalytic properties of $\text{Ru}/\text{AlOOH-SiO}_2$ catalysts for benzene selective hydrogenation. *Catal. Sci. Technol.* **2018**, *8*, 1435–1446. [[CrossRef](#)]
2. Spod, H.; Lucas, M.; Claus, P. Selective hydrogenation of benzene to cyclohexene over $2\text{Ru}/\text{La}_2\text{O}_3\text{-ZnO}$ catalyst without additional modifiers. *ChemCatChem* **2016**, *8*, 2659–2666. [[CrossRef](#)]
3. Liu, J.; Xu, S.; Bing, W.; Wang, F.; Li, C.; Wei, M.; Evans, D.G.; Duan, X. Cu-decorated Ru catalysts supported on layered double hydroxides for selective benzene hydrogenation to cyclohexene. *ChemCatChem* **2015**, *7*, 846–855. [[CrossRef](#)]
4. Yan, X.; Zhang, Q.; Zhu, M.; Wang, Z. Selective hydrogenation of benzene to cyclohexene over $\text{Ru-Zn}/\text{ZrO}_2$ catalysts prepared by a two-step impregnation method. *J. Mol. Catal. A Chem.* **2016**, *413*, 85–93. [[CrossRef](#)]
5. Alimardanov, K.M.; Sadygov, O.A.; Garibov, N.I.; Abbasov, M.F.; Abdullaeva, M.Y.; Dzharfarova, N.A. Liquid-phase catalytic oxidation of $\text{C}_6\text{-C}_7$ cycloolefins into carboxylic acids in a pseudohomogeneous system. *Russ. J. Appl. Chem.* **2011**, *84*, 236–242. [[CrossRef](#)]
6. Saha, D.; Hazra, D.K.; Maity, T.; Koner, S. Heterometallic metal-organic frameworks that catalyze two different reactions sequentially. *Inorg. Chem.* **2016**, *55*, 5729–5731. [[CrossRef](#)] [[PubMed](#)]
7. Damm, M.; Gutmann, B.; Kappe, C.O. Continuous-flow synthesis of adipic acid from cyclohexene using hydrogen peroxide in high-temperature explosive regimes. *ChemSusChem* **2013**, *6*, 978–982. [[CrossRef](#)]
8. Chen, B.H.; Liu, W.; Li, A.; Liu, Y.J.; Chao, Z.S. A simple and convenient approach for preparing core-shell-like silica@nickel species nanoparticles: Highly efficient and stable catalyst for the dehydrogenation of 1,2-cyclohexanediol to catechol. *Dalton T.* **2015**, *44*, 1023–1038. [[CrossRef](#)]
9. Paushkin, Y.M.; Nizova, S.A.; Stytsenko, V.D.; Belov, P.S.; Rozovskii, A.Y.; D'Yakonov, A.Y. Preparation of pyrocatechol and its alkyl and aryl derivatives. *Dokl. Chem.* **1983**, *271*, 217–219.
10. Zhou, Z.Z.; Liu, M.; Lv, L.; Li, C.J. Silver(I)-catalyzed widely applicable aerobic 1,2-diol oxidative cleavage. *Angew. Chem. Int. Edit.* **2018**, *57*, 2616–2620. [[CrossRef](#)]
11. Ghosh, S.; Acharyya, S.S.; Adak, S.; Konathala, L.N.S.; Sasaki, T.; Bal, R. Selective oxidation of cyclohexene to adipic acid over silver supported tungsten oxide nanostructured catalysts. *Green Chem.* **2014**, *16*, 2826–2834. [[CrossRef](#)]
12. Zhang, C.; Qi, J.; Xing, J.; Tang, S.F.; Song, L.; Sun, Y.; Zhang, C.; Xin, H.; Li, X. An investigation on the aqueous-phase hydrodeoxygenation of various methoxy-substituted lignin monomers on Pd/C and HZSM-5 catalysts. *RSC Adv.* **2016**, *6*, 104398–104406. [[CrossRef](#)]
13. Cho, C.S.; Oh, S.G. A new ruthenium-catalyzed approach for quinoxalines from ortho-phenylenediamines and vicinal-diols. *Tetrahedron Lett.* **2006**, *47*, 5633–5636. [[CrossRef](#)]
14. Lee, H.; Yi, C.S. Catalytic synthesis of substituted indoles and quinolines from the dehydrative C-H coupling of arylamines with 1,2- and 1,3-Diols. *Organometallics* **2016**, *35*, 1973–1977. [[CrossRef](#)] [[PubMed](#)]
15. Xiong, B.; Zhang, S.D.; Chen, L.; Li, B.; Jiang, H.F.; Zhang, M. An annulative transfer hydrogenation strategy enables straightforward access to tetrahydro fused-pyrazine derivatives. *Chem. Commun.* **2016**, *52*, 10636–10639. [[CrossRef](#)] [[PubMed](#)]

16. Bierenstiel, M.; D'Hondt, P.J.; Schlaf, M. Investigations into the selective oxidation of vicinal diols to α -hydroxy ketones with the $\text{NaBrO}_3/\text{NaHSO}_3$ reagent: pH dependence, stoichiometry, substrates and origin of selectivity. *Tetrahedron* **2005**, *61*, 4911–4917. [CrossRef]
17. William, J.M.; Kuriyama, M.; Onomura, O. An efficient method for selective oxidation of 1,2-Diols in water catalyzed by Me_2SnCl_2 . *RSC. Adv.* **2013**, *3*, 19247–19250. [CrossRef]
18. Obara, N.; Hirasawa, S.; Tamura, M.; Nakagawa, Y.; Tomishige, K. Oxidative cleavage of vicinal diols with the combination of platinum and vanadium catalysts and molecular oxygen. *ChemCatChem* **2016**, *8*, 1732–1738. [CrossRef]
19. Hsiao, M.C.; Liu, S.T. Polymer supported vanadium complexes as catalysts for the oxidation of alkenes in water. *Catal. Lett.* **2010**, *139*, 61–66. [CrossRef]
20. Verma, S.; Jain, S.L.; Sain, B. Poly(ethylene glycol) embedded potassium tribromide ($\text{PEG}\bullet\text{KBr}_3$) as a recyclable catalyst for oxidation of alcohols. *Ind. Eng. Chem. Res.* **2011**, *50*, 5862–5865. [CrossRef]
21. Khenkin, A.M.; Neumann, R. Aerobic oxidation of vicinal diols catalyzed by an anderson-type polyoxometalate, $[\text{IMo}_6\text{O}_{24}]^{5-}$. *Adv. Synth. Catal.* **2002**, *344*, 1017–1021. [CrossRef]
22. Sato, H.; Tamura, M.; Nakagawa, Y.; Tomishige, K. Synthesis of alpha-hydroxy ketones from vicinal diols by selective dehydrogenation over Ir-ReO_x/SiO₂ catalyst. *Chem. Lett.* **2014**, *43*, 334–336. [CrossRef]
23. Zhou, G.D.; Guo, X.H.; Lu, X.J.; Li, Y.N.; Cheng, T.X.; Li, W.X.; Zhen, K.J. MgO-Supported Cu₂PmO₁₁VO₄₀ Catalyst for Oxidative Dehydrogenation of n-Hexanol to n-Hexanal. *Chin. J. Catal.* **2005**, *26*, 389–392.
24. Ji, D.; Zhu, W.; Wang, Z.; Wang, G. Dehydrogenation of cyclohexanol on Cu-ZnO/SiO₂ catalysts: The role of copper species. *Catal. Commun.* **2007**, *8*, 1891–1895. [CrossRef]
25. Fridman, V.Z.; Davydov, A.A.; Titievsky, K. Dehydrogenation of cyclohexanol on copper-containing catalysts: II. The pathways of the cyclohexanol dehydrogenation reaction to cyclohexanone on copper-active sites in oxidation state Cu⁰ and Cu⁺. *J. Catal.* **2004**, *222*, 545–557. [CrossRef]
26. Fridman, V.Z.; Davydov, A.A. Dehydrogenation of cyclohexanol on copper-containing catalysts: I. The influence of the oxidation state of copper on the activity of copper sites. *J. Catal.* **2000**, *195*, 20–30. [CrossRef]
27. Luna, A.; Alcamí, M.; Mó, O.; Máñez, M. Cu⁺ reactivity trends in sp, sp², and sp³ nitrogen, phosphorus, and arsenic containing bases. *Int. J. Mass. Spectrom* **2000**, *201*, 215–231. [CrossRef]
28. Trost, B.M.; Schroeder, G.M. Cyclic 1,2-diketones as building blocks for asymmetric synthesis of cycloalkenones. *J. Am. Chem. Soc.* **2000**, *122*, 3785–3786. [CrossRef]
29. Svennebring, A.; Nilsson, P.; Larhed, M. Microwave-accelerated spiro-cyclizations of o-halobenzyl cyclohexenyl ethers by palladium (0) catalysis. *J. Org. Chem.* **2007**, *72*, 5851–5854. [CrossRef]
30. Jeena, V.; Robinson, R.S. Green oxidations: Titanium dioxide induced tandem oxidation coupling reactions. *Beilstein. J. Org. Chem.* **2009**, *5*, 24. [CrossRef]
31. Araki, Y.; Miyawaki, A.; Miyashita, T.; Mizutani, M.; Hirai, N.; Todoroki, Y. A new non-azole inhibitor of ABA 8'-hydroxylase: Effect of the hydroxyl group substituted for geminal methyl groups in the six-membered ring. *Bioorg. Med. Chem. Lett.* **2006**, *16*, 3302–3305. [CrossRef]
32. Cleghorn, L.A.T.; Cooper, I.R.; Fishwick, C.W.G.; Grigg, R.; MacLachlan, W.S.; Rasparini, M.; Sridharan, V. Three-component bimetallic (Pd/In) mediated cascade allylation of C=X functionality: Part 1. Scope and class 1 examples with aldehydes and ketones. *J. Organomet. Chem.* **2003**, *687*, 483–493. [CrossRef]
33. Frisch, M.J.; Trucks, G.W.; Schlegel, H.B.; Scuseria, G.E.; Robb, M.A.; Cheeseman, J.R.; Scalmani, G.; Barone, V.; Petersson, G.A.; Nakatsuji, H.; et al. *Gaussian 09, Revision C. 01*; Gaussian, Inc.: Wallingford, CT, USA, 2016; Available online: <http://gaussian.com/g09citation/> (accessed on 9 February 2019).
34. Tomasi, J.; Mennucci, B.; Cancès, E. The IEF version of the PCM solvation method: an overview of a new method addressed to study molecular solutes at the QM ab initio level. *J. Mol. Struct.* **1999**, *464*, 211–226. [CrossRef]
35. Xu, G.Y.; Guo, J.H.; Qu, Y.C.; Zhang, Y.; Fu, Y.; Guo, Q.X. Selective hydrodeoxygenation of lignin-derived phenols to alkyl cyclohexanols over a Ru-solid base bifunctional catalyst. *Green Chem.* **2016**, *18*, 5510–5517. [CrossRef]
36. Song, W.; Liu, Y.; Baráth, E.; Zhao, C.; Lercher, J.A. Synergistic effects of Ni and acid sites for hydrogenation and C-O bond cleavage of substituted phenols. *Green Chem.* **2015**, *17*, 1204–1218. [CrossRef]

37. Liu, T.; Ma, P.C.; Yu, J.K.; Li, L.; Liu, X.; Ma, B. Preparation of MgO by Thermal Decomposition of $Mg(OH)_2$. *J. Chin. Ceram. Soc.* **2010**, *38*, 1337–1340.
38. Meda, L.; Cerofolini, G.F. A decomposition procedure for the determination of copper oxidation states in Cu-zeolites by XPS. *Surf. Interface Anal.* **2004**, *36*, 756–759. [[CrossRef](#)]



© 2019 by the authors. Licensee MDPI, Basel, Switzerland. This article is an open access article distributed under the terms and conditions of the Creative Commons Attribution (CC BY) license (<http://creativecommons.org/licenses/by/4.0/>).